Available online at www.sciencedirect.com
ScienceDirect
Journal of Power Sources 165 (2007) 386–392
JOURNAL OF POWER SOURCES
www.elsevier.com/locate/jpowsour

Improvement in electrochemical performance of V_2O_5 by Cu doping

Yingjin Wei [a,b,*], Chang-Wan Ryu [b], Kwang-Bum Kim [b]

[a] College of Materials Science and Engineering, Jilin University, Changchun 130023, China
[b] Division of Material Science and Engineering, Yonsei University, 134 Shinchon-dong, Seodaemoon-gu, Seoul 120-749, Republic of Korea

Received 7 June 2006; received in revised form 30 November 2006; accepted 11 December 2006
Available online 16 December 2006

Abstract

$Cu_{0.04}V_2O_5$ was prepared by a precipitation method followed by heat treatment at 300 and 600 °C. The material prepared at 300 °C showed porous morphology, whereas that prepared at 600 °C was highly crystalline. X-ray diffraction, Raman scattering and Fourier transform infrared spectroscopy showed both materials exhibiting the same structure as that of V_2O_5, with a slight lattice expansion. X-ray absorption spectroscopy confirmed the presence of V^{4+} cations in $Cu_{0.04}V_2O_5$, which would increase the electronic conductivity of V_2O_5. $Cu_{0.04}V_2O_5$ showed better electrochemical performance than V_2O_5 because of its high electronic conductivity and good structural stability. The material prepared at 600 °C delivered a reversible discharge capacity over 160 mAh g^{-1} after 60 cycles at a *C* rate of *C*/5.6. The material prepared at 300 °C showed good high-rate performance, which delivered a reversible capacity ~100 mAh g^{-1} when cycled at *C*/1.9. The discrepancy in the rate performance of $Cu_{0.04}V_2O_5$ was attributed to the morphology of materials.

Keywords: V_2O_5; Cation doping; Structural property; Electrochemical performance

1. Introduction

Vanadium based oxides such as V_2O_5, LiV_3O_8, V_6O_{13}, and some transitional metal vanadates (MeV_2O_6) have been considered as cathode materials for rechargeable lithium batteries because of their high energy densities, low price and good safety properties [1–9]. Among these vanadium oxides, V_2O_5 has gained the most attention for more than two decades [10]. V_2O_5 crystallizes in a simple orthorhombic structure with space group *Pmmn*. Each [VO_6] octahedron contains a central vanadium atom, which bonded to two vanadyl (O^1), three chain (O^2) and one bridge (O^3) oxygen atoms. The vanadium atoms experience distinct displacements away from the centers of [VO_6] octahedron. Due to these displacements, the remaining basic units finally become [VO_5] square pyramids rather than regular octahedron. The V_2O_5 layer is built up from these [VO_5] pyramids by sharing edges and corners [11].

The layered structure of V_2O_5 makes it much favorable for Li^+ insertion and extraction. A main obstacle that hampers the practical applications of V_2O_5 is the fast capacity fading during cycling. This fast capacity fading has been attributed to some reasons such as the low electronic conductivity and Li^+ diffusivity of the material [12] as well as its structural collapse during long term cycling [13]. Recently, intensive work has been done to overcome these shortcomings encountered in the applications of V_2O_5. Smyrl and colleagues prepared V_2O_5 aero- and xero-gel materials, which were highly porous and had large effective surface area. These materials showed large Li^+ capacities ($x > 3$ in $Li_xV_2O_5$) [14]. However, their capacity retention was still unsatisfying. As an improvement, cation doped $M_xV_2O_5$ (M = Ag, Cu, etc.) showed better cycling performance than the un-doped aero or xero-gel V_2O_5 [15–17]. Physical property measurements demonstrated that the electronic conductivities of $M_xV_2O_5$ were 10–100 times higher than that of V_2O_5 (≈10^{-3} S cm^{-1}), giving rise to the good electrochemical performance of the materials [15]. Furthermore, it was pointed out that the [MO_6] octahedral chains formed in the crystal frameworks increased the material's structural stability, which might prevent the structural collapse of the material during charge/discharge cycling [13].

* Corresponding author at: College of Materials Science and Engineering, Jilin University, Changchun 130023, China. Tel.: +86 431 85168444; fax: +86 431 85168015.
E-mail address: yjwei@jlu.edu.cn (Y. Wei).

0378-7753/$ – see front matter © 2006 Elsevier B.V. All rights reserved.
doi:10.1016/j.jpowsour.2006.12.016

Cation doped V_2O_5 has been studied by several groups [15–19]. These pioneer works, however, focused mainly on the preparation and electrochemical properties of aero- or xerogel $M_xV_2O_5$ amorphous materials. In this work, we prepared crystalline Cu doped V_2O_5 at different temperatures. The structural properties of the materials were characterized, and their electrochemical properties were studied in the potential region 4.0–2.0 V.

2. Experimental

Cu doped V_2O_5 were prepared using V_2O_5 and $Cu(NO_3)_2$ as starting materials. About 0.02 mol of V_2O_5 was added into 100 ml water, followed by slowly dropping ammonia water under constant stirring to get a yellowish solution. Then 0.001 mol of $Cu(NO_3)_2$ was added and dissolved. The solution pH was adjusted to 8.5 by addition of ammonia solution. The formed precipitate was filtered and washed to neutral pH, then dried at 100 °C for 3 h. This solid precursor was divided into two parts and subjected to calcinations at 300 °C (denoted as sample-A) and 600 °C (denoted as sample-B) for 5 h at the ambient condition in muffle furnace to get the final products.

Inductively coupled plasma (ICP) measurement was performed using a GBC Itegra XL instrument to analyze the composition of the samples. The morphology of the materials was investigated by scanning electron microscopy (SEM, FEI-Company SIRION^{TM}). X-ray diffraction (XRD) was performed on a Rigaku RINT/Dmax-2500 instrument with Cu Kα radiation. The diffraction data were collected in the 2θ region 10–70° with a step of 0.02°. Raman scattering was collected on a LabRam (Jobin-Yvon) micro-Raman instrument. The excitation light source was an argon-ion laser with $\lambda = 514.5$ nm. A low light power of 0.5 mW was used to avoid photodecomposition of the materials. The acquisition time of Raman scattering was 30 s. Fourier transform infrared (FTIR) spectroscopy was recorded on a Spectrum One B spectrometer (PE Company) in the region of 400–4000 cm^{-1}. The vanadium oxidation state of the materials was determined by V K-edge X-ray absorption near edge spectroscopy (XANES) at the beamline 7C at Pohang Light Source. The spectrum was recorded in the region of 5460–5500 eV, with a step of 0.2 eV and 1 s integration time. The XANES data were calibrated using the first inflection point of the spectrum of V foil, *i.e.* 5465 eV.

The working electrode was prepared using a mixture of active material (82 wt.%), carbon black (12 wt.%) and PVDF (6 wt.%) dissolved in *N*-methylpyrrolidone. The slurry mixture was pasted on a polished Al foil, followed by drying at 120 °C for 10 h. A three-electrode electrochemical cell was used with a Li foil and a Li wire as the counter and reference electrodes, respectively. The electrolyte was a solution of 1 M $LiClO_4$ dissolved in propylene carbonate (PC). Cyclic voltammogram (CV) was collected on a VMP2 Multichannel Potentiostat electrochemical interface at a sweep rate of 0.02 mV s^{-1} in the potential region 2.1–4.0 V. The charge/discharge experiment was performed on a battery cycler (WonATech WBCS-300) over the potential region of 4.0–2.0 V. All of the electrochemical experiments were performed in an argon filled glove box.

3. Results and discussion

Fig. 1 shows the SEM photographs of the samples calcined at 300 (sample-A) and 600 °C (sample-B). A significant difference in the material's morphology was observed. The sample-A contains irregular flake-shaped particles with thickness of around 500 nm and a geometric surface area of several μm^2 (Fig. 1a). Fig. 1b is the magnified picture of Fig. 1a and shows the porous nature of the material. On the contrary, the material prepared at 600 °C (Fig. 1c) was made up of well-crystallized spherical particles. The geometric particle size of the material was about

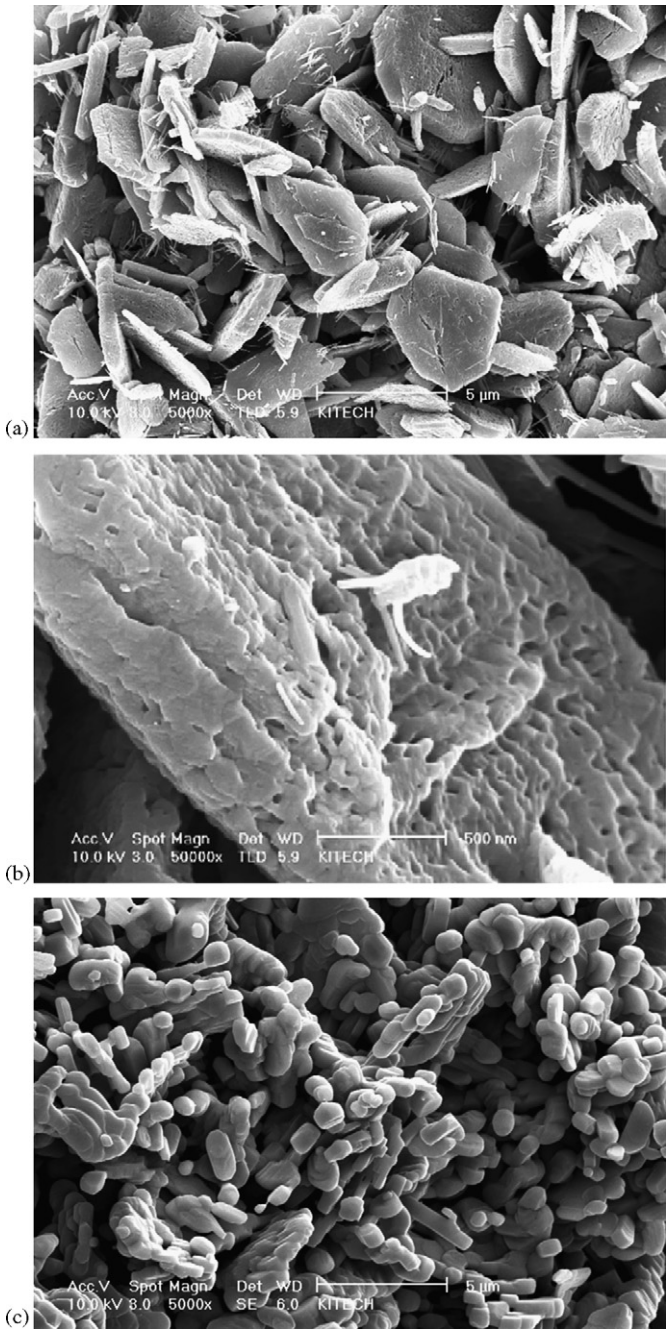

Fig. 1. The SEM photographs of $Cu_{0.04}V_2O_5$ prepared at 300 °C (a, 5000×; b, 50,000×) and 600 °C (c, 5000×).

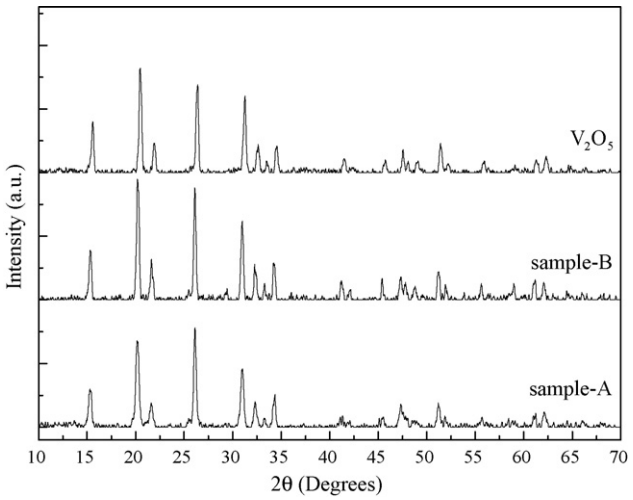

Fig. 2. The X-ray diffraction patterns of $Cu_{0.04}V_2O_5$ and V_2O_5.

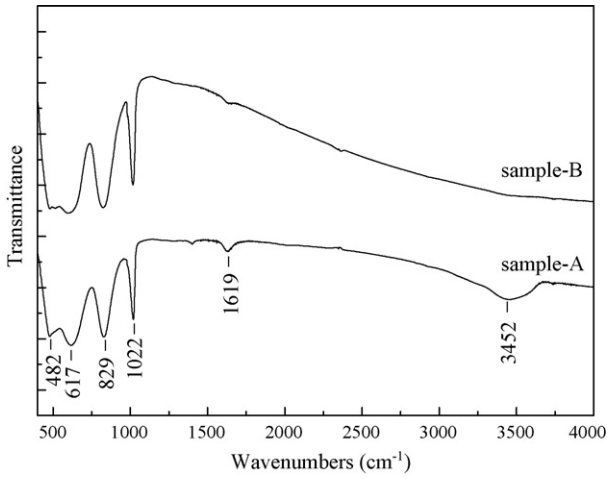

Fig. 4. The FTIR patterns of the $Cu_{0.04}V_2O_5$ samples.

1–2 μm. Observed agglomeration of the particles was attributed to the sintering of the material at high temperatures. The numerous small pores in the particles of sample-A provide a large effective surface area and very thin pore-walls to the material, which may influence the material's electrochemical properties as will be shown below.

ICP analysis showed a Cu:V ratio as 1:50 in both calcined samples, corresponding to the formula of $Cu_{0.04}V_2O_5$. Fig. 2 displays the XRD patterns of the $Cu_{0.04}V_2O_5$ samples, along with that of crystalline V_2O_5. Both materials exhibited the orthorhombic structure as that of V_2O_5. The lattice parameters were calculated by the least-squares refinement method, which were $a = 11.52$ Å, $b = 3.57$ Å, $c = 4.39$ Å for the sample-A and $a = 11.54$ Å, $b = 3.57$ Å, $c = 4.38$ Å for the sample-B. Compared with the values of crystalline V_2O_5 ($a = 11.46$ Å, $b = 3.55$ Å, $c = 4.35$ Å), it is found that Cu doping in V_2O_5 induced a slight expansion ($\Delta V/V \approx 2\%$) in the material's lattice volume. The increase in the unit cell parameters was a clear evidence of doping of Cu in V_2O_5.

Raman patterns of the $Cu_{0.04}V_2O_5$ sample-A and -B are illustrated in Fig. 3. Both samples exhibit the typical Raman pattern as that of V_2O_5 [20]. But the band intensities of sample-A are a little lower than those of sample-B, which may be attributed to the low crystallinity of the material. No extra Raman bands corresponding to Cu–O vibrations were observed probably because of the low Cu content in the materials. The Raman bands recorded at 995, 701, and 528 cm^{-1} are assigned to the stretching vibrations of the shortest V–O^1 bond, bridging V–O^3 bond and chaining V–O^2 bond, respectively. The bands at 404 and 284 cm^{-1} correspond to the bending vibrations of the V–O^1 bond. And the bands at 482 and 303 cm^{-1} are assigned to the bending vibrations of the V–O^3 and V–O^2 bonds, respectively. There are other two Raman bands recorded at 197 and 144 cm^{-1}, which correspond to the $[VO_5]$–$[VO_5]$ vibrations. These vibrations observed at low wavenumbers are attributed to the heavy $[VO_5]$ units. Fig. 4 shows the FTIR spectra of the $Cu_{0.04}V_2O_5$ materials. The IR bands at 1022 and 482 cm^{-1} are attributed to the V–O^1 vibrations, and the bands at 829 and 617 cm^{-1} correspond to the V–O^3 and V–O^2 vibrations, respectively [21]. Beside these, two weak IR bands observed at 1619 and 3452 cm^{-1} for the material prepared at 300 °C are assigned to the residual water in the material. These bands were absent in the sample prepared at 600 °C.

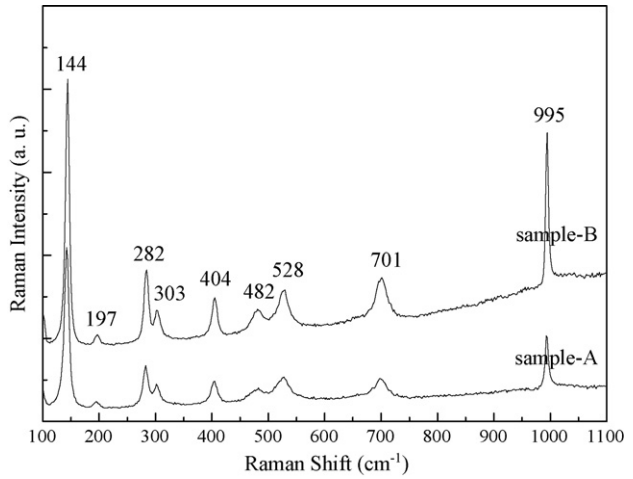

Fig. 3. The Raman patterns of the $Cu_{0.04}V_2O_5$ samples.

Due to the high sensitivity to the electronic structures of absorbing atoms, XANES is a powerful technique to study the oxidation states of materials. A comparison of the normalized V K-edge XANES of $Cu_{0.04}V_2O_5$, along with that of crystalline V_2O_5 is shown in Fig. 5. It is observed that $Cu_{0.04}V_2O_5$ exhibited the similar XANES profile as that of crystalline V_2O_5. This indicates that the local environments around the V atoms are similar in both cases. However, the absorption main edge for $Cu_{0.04}V_2O_5$ slightly shifted toward lower energies with respect to V_2O_5. This indicates that the V oxidation states in $Cu_{0.04}V_2O_5$ were lower than that of +5 in pure V_2O_5. In other words, a few V^{4+} cations were generated by Cu doping in V_2O_5. The formation of V^{4+} cations would result in higher electronic conductivities for $Cu_{0.04}V_2O_5$ than for V_2O_5. It has been reported that the conductivity mechanism of V_2O_5 is attributed to the small-polaron theory. With Cu doping in V_2O_5, more small polarons will be generated by coupling the negative charges

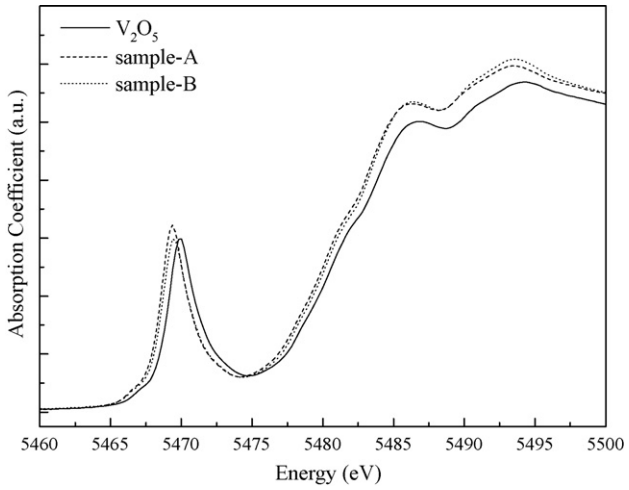

Fig. 5. The XANES patterns of $Cu_{0.04}V_2O_5$ and V_2O_5.

residing on the V^{4+} cations, as well as the lattice deformation induced by the Cu^{2+} cations, which leads to a higher electronic conductivity [15,22]. The enhancement in the material's electronic conductivity was expected to improve its electrochemical performance.

The cyclic voltammograms of the sample-A and -B and crystalline V_2O_5 during the first cycle are shown in Fig. 6. All of the samples exhibited three well-defined reduction peaks at ~3.35, 3.17 and 2.31 V, corresponding to the formation of the ε, δ and γ phases, respectively [23]. More than three peaks appeared at ~2.46, 2.60, 2.85, 3.30, 3.44, 3.52 and 3.65 V in the anodic region. This indicates complex structural changes taking place in the cathode material during the oxidation process. However, the current peaks at 2.46, 3.30 and 3.44 V for $Cu_{0.04}V_2O_5$ were much weaker than those of V_2O_5. This indicates that the formation of some phases was significantly depressed by Cu doping. Therefore, $Cu_{0.04}V_2O_5$ was expected to show better cycling performance than pure V_2O_5 because of the presence of less number of phases. Furthermore, a pair of weak redox peaks appearing at around 3.0 V for the $Cu_{0.04}V_2O_5$ samples were absent for V_2O_5. These extra peaks were assigned to the Cu^{2+}/Cu redox couple, whose existence has been observed for Cu doped V_2O_5 xero-gels [15].

Galvanostatic charge/discharge cycling of V_2O_5 and $Cu_{0.04}V_2O_5$ was carried out in the potential region 4.0–2.0 V at a current density of 100 mA g^{-1}. This current density corresponds to the *C* rate of *C*/5.6, assuming that the full capacity of V_2O_5 to be four equivalents of lithium per mole of material, etc. 560 mAh g^{-1}. Fig. 7 shows the discharge/charge potential profiles of the first cycle. All of the samples exhibited the open circuit potentials at ~3.5 V. The discharge profiles comprised three voltage plateaus at ~3.4, 3.2 and 2.3 V, whereas the subsequent charge process exhibited S-shaped profiles. The discharge/charge capacities of the samples were recorded as 246/243 (V_2O_5), 260/254 (sample-A) and 229/211 mAh g^{-1} (sample-B), respectively. Discharge capacities *versus* cycle numbers of the three samples were plotted in Fig. 8. All of the samples showed fast capacity fading in the initial cycles.

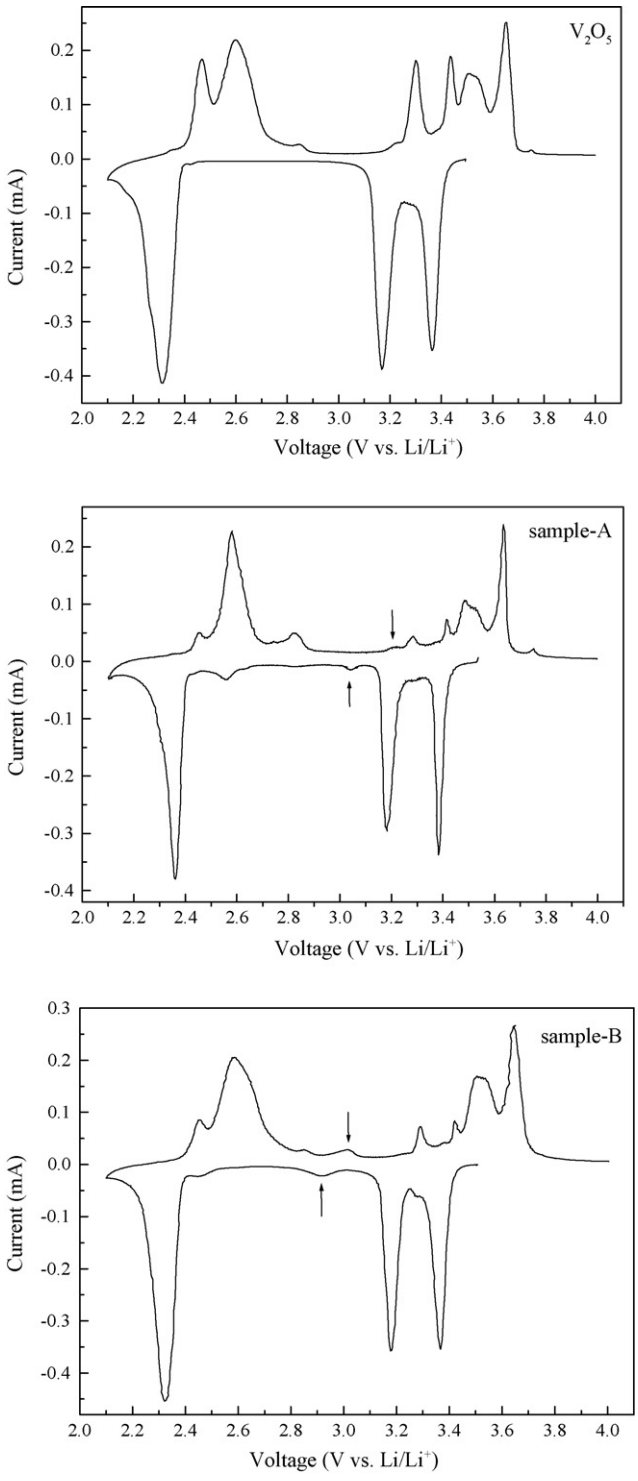

Fig. 6. The cyclic voltammograms of $Cu_{0.04}V_2O_5$ and V_2O_5 during the first cycle, the arrows denoted the Cu^{2+}/Cu redox couple.

V_2O_5 exhibited similar cycling performance as that of $Cu_{0.04}V_2O_5$ prepared at 300 °C. However, the capacity fading of V_2O_5 became faster after 40 cycles. It is seen that Cu doping significantly improved the electrochemical performance of V_2O_5. Especially, $Cu_{0.04}V_2O_5$ prepared at 600 °C showed much better capacity retention than the other samples, which maintained a discharge capacity over 160 mAh g^{-1} after 60 cycles.

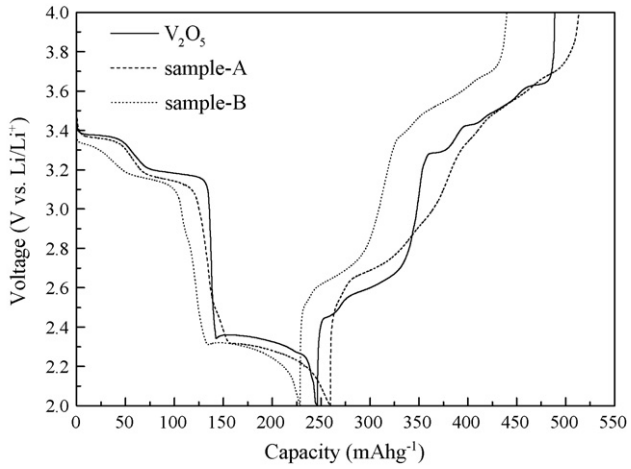

Fig. 7. The discharge/charge potential profiles of $Cu_{0.04}V_2O_5$ and V_2O_5 during the first cycle.

$Cu_{0.04}V_2O_5$ prepared at 300 °C showed faster capacity fading, but its discharge capacities in the initial 35 cycles were larger than that prepared at 600 °C.

Fig. 9 shows the discharge potential profiles of the sample-A and -B and V_2O_5 at 2, 20, 40 and 60th cycle. All of the samples exhibited well-defined S-shaped potential profiles at the second cycle. The shape of the potential profiles of the sample-A and -B did not change much with further cycling up to 60 cycles. This indicates good structural stability of $Cu_{0.04}V_2O_5$ during long term cycling. It is noticed that even though the sample-A and pure V_2O_5 had almost the same discharge capacities in the initial 40 cycles, their potential profiles were different because of the difference in the material's microstructure. The potential profiles of V_2O_5 became almost slope-like after 20 cycles, which indicates a poor crystallinity of the material. Further, the fast capacity fading of V_2O_5 after 40 cycles might be caused by the structural collapse of the already poorly crystalline material. Fig. 10 displays the XRD patterns of sample-A and V_2O_5 at the end of discharge after 60 cycles. It is seen from the figure that the XRD peaks of the discharged $Cu_{0.04}V_2O_5$ was much

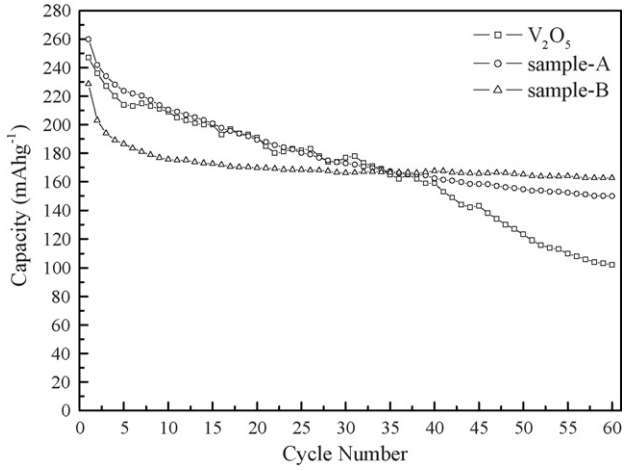

Fig. 8. The cycling performance of $Cu_{0.04}V_2O_5$ and V_2O_5 performed at the rate of *C*/5.6.

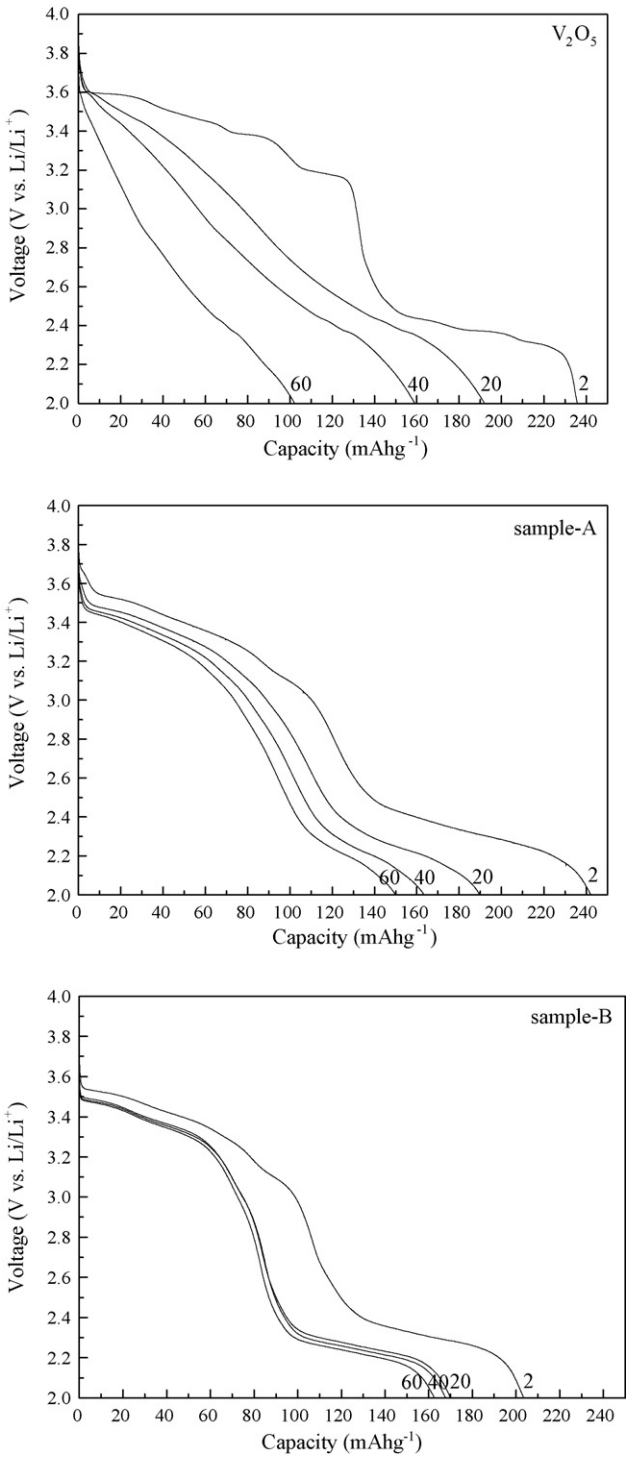

Fig. 9. The discharge potential profiles of $Cu_{0.04}V_2O_5$ and V_2O_5 at 2, 20, 40 and 60th cycle performed at the rate of *C*/5.6.

sharper and higher than those of pure V_2O_5. This indicates that Cu doping in V_2O_5 improved the material's structural stability, leading to the better cycling performance of the doped materials.

Fig. 11 compares the cycling performance of sample-A and -B at high rates, *viz.*, *C*/2.8 (200 mAh g^{-1}) and *C*/1.9 (300 mAh g^{-1}), respectively. The sample-A exhibited good potentials for battery use at high-rate conditions. At a very high rate of *C*/1.9, the material still showed good cycling

Table 1
A comparison of the electrochemical properties of crystalline $M_xV_2O_5$ with some amorphous $M_xV_2O_5$ reported in early works

	$M_xV_2O_5$			
	Amorphous phase		Crystalline phase	
	$Cu_{0.05}V_2O_5$ [15]	$Mn_{0.04}V_2O_5$ [19]	$Cu_{0.04}V_2O_5$[a]	$Cr_{0.11}V_2O_{5.16}$ [24]
Reversible capacity	130 mAh g^{-1}	90 mAh g^{-1}	160 mAh g^{-1}	250 mAh g^{-1}
Conditions	*C*/4, 4.0–1.5 V	*C*/11.2, 4.0–2.0 V	*C*/2.8, 4.0–2.0 V	*C*/5, 4.0–1.5 V

[a] This work.

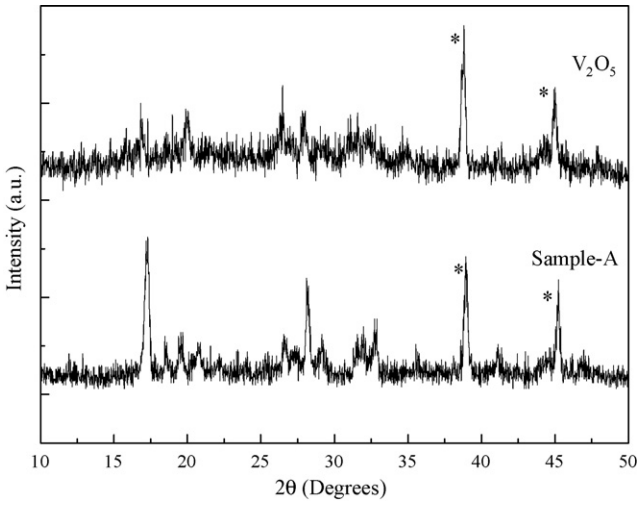

Fig. 10. The XRD patterns of $Cu_{0.04}V_2O_5$ (sample-A) and V_2O_5 at the end of discharge after 60 cycles. The peaks marked by "*" are assigned to the Al foils of the cathode electrodes.

performance, which maintained a reversible discharge capacity ~100 mAh g^{-1} over 100 cycles. Contrarily, the sample-B showed bad cycling performance at high-rate conditions. When the *C* rate was raised to *C*/2.8, the discharge capacities decreased rapidly and were lower than 40 mAh g^{-1} after 40 cycles.

It is concluded from Figs. 8 and 11 that the sample-B showed good low-rate performance, whereas the sample-A exhibited good high-rate performance. This discrepancy in the rate performance of sample-A and -B might be attributed to the morphology

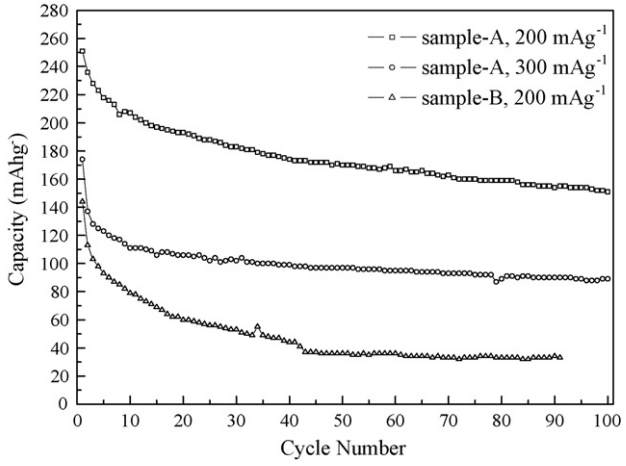

Fig. 11. The cycling performance of the $Cu_{0.04}V_2O_5$ samples performed at the rates of *C*/2.8 and *C*/1.9.

of the materials. At low rates, the Li^+ diffusion was efficient in both samples. The high crystallinity of sample-B could maintain a more stabled structure, therefore resulted in good low-rate performance. At high rates, the Li^+ diffusion in sample-B might be severely limited by its large particle size, resulting in bad high-rate performance. Contrarily, the sample-A still showed good cycling performance at such high rates because of its highly porous morphology, which provides a large effective surface area to the material. In addition, the thin pore-walls of the particles, which average size was estimated less than 100 nm from SEM, provided a very short diffusion length for lithium intercalation. These advantages led to the good high-rate performance of sample-A. However, it is strange to see that the cycling performance of sample-A became better and better with the *C* rate increase from *C*/5.6 to *C*/1.9, especially after the initial 20 cycles. At present we are not able to give a convinced explanation to this phenomenon.

4. Conclusions

In this study, we applied a precipitation method to prepare the precursor, followed by heat treatment at 300 and 600 °C to obtain crystalline $Cu_{0.04}V_2O_5$ cathode materials. Both materials had the same crystal structure as that of V_2O_5 but with a slight lattice expansion. XANES confirmed the presence of V^{4+} cations in $Cu_{0.04}V_2O_5$, which would increase the electronic conductivity of V_2O_5. $Cu_{0.04}V_2O_5$ showed better cycling performance than pure V_2O_5 because of its high electronic conductivity and good structural stability. $Cu_{0.04}V_2O_5$ prepared at 600 °C showed good low-rate performance, whereas the material prepared at 300 °C exhibited good high-rate performance. The discrepancy in the rate performance was attributed to the morphology of the materials. Table 1 compares the electrochemical data of crystalline $M_xV_2O_5$ (M = Cu, Cr) with some amorphous $M_xV_2O_5$ (M = Cu, Mn) reported in early works. These data suggests that crystalline $M_xV_2O_5$ are potential cathode materials for lithium batteries, provided they are properly prepared. Future work should be done to study the electrochemical and physical properties of crystalline $Cu_xV_2O_5$ with different Cu contents to optimize the electrochemical performance of these materials.

Acknowledgement

This work was supported by the Ministry of Education and Human Resources Development, the Ministry of Commerce, Industry and Energy and the Ministry of Labor through the fos-

tering project of the Lab of Excellency and by the Ministry of Information and Communication of KOREA (Support Project of University Information Technology Research Center supervised by KIPA). Partial work was supported by the special funds for major state basic research project (973) of China under the Grant 2002CB211802.

References

[1] A.N. Mansour, P.H. Smith, W.M. Baker, M. Balasubramanian, J. McBreen, J. Electrochem. Soc. 150 (2003) A403.
[2] Y.-Q. Chu, Q.-Z. Qin, Chem. Mater. 14 (2002) 3152.
[3] G.Q. Liu, N. Xu, C.L. Zeng, K. Yang, Mater. Res. Bull. 37 (2002) 727.
[4] L.A. de Piccotto, K.T. Adendorff, D.C. Liles, M. Thackeray, Solid State Ionics 62 (1993) 297.
[5] Y.J. Wei, K.-W. Nam, G. Chen, C.-W. Ryu, K.-B. Kim, Solid State Ionics 176 (2005) 2243.
[6] G. Yang, G. Wang, W.H. Hou, J. Phys. Chem. B 109 (2005) 11186.
[7] K. West, B.Z. Christiansen, S. Skaarup, Y. Saidi, J. Barker, I.I. Olsen, R. Pynenburg, R. Koksbang, J. Electrochem. Soc. 143 (1996) 820.
[8] F. Zhang, M.S. Whittingham, Electrochem. Commun. 2 (2000) 69.
[9] M. Inagaki, T. Morishita, M. Hirano, V. Gupta, T. Nakajima, Solid State Ionics 156 (2003) 275.
[10] D.W. Murphy, P.A. Christian, Science 205 (1979) 651.
[11] O. Šipr, A. Šimůnek, S. Bocharov, T. Kirchner, G. Dräger, Phys. Rev. B 60 (1999) 14115.
[12] B.B. Owens, S. Passerini, W.H. Smyrl, Electrochim. Acta 45 (1999) 215.
[13] G. Grégoire, N. Baffier, A. Kahn-harari, J.-C. Badot, J. Mater. Chem. 8 (1998) 2103.
[14] D.B. Le, S. Passerini, J. Guo, J. Ressler, B.B. Owens, W.H. Smyrl, J. Electrochem. Soc. 143 (1996) 2099.
[15] F. Coustier, J. Hill, B.B. Owens, S. Passerini, W.H. Smyrl, J. Electrochem. Soc. 146 (1999) 1355.
[16] F. Coustier, G. Jarero, S. Passerini, W.H. Smyrl, J. Power Sources 83 (1999) 9.
[17] F. Coustier, S. Passerini, W.H. Smyrl, Solid State Ionics 100 (1997) 247.
[18] J.H. Choi, H.K. Park, Electrochim. Acta 50 (2004) 405.
[19] H.K. Park, Solid State Ionics 176 (2005) 307.
[20] S.-H. Lee, H.M. Cheong, M.J. Seong, P. Liu, C.E. Tracy, A. Mascarenhas, J.R. Pitts, S.K. Deb, Solid State Ionics 165 (2003) 111.
[21] J.M. Lee, H.-S. Hwang, W.-I. Cho, B. -Won Cho, K.Y. Kim, J. Power Sources 136 (2004) 122.
[22] J. Bullot, O. Gallais, M. Gauthier, J. Livage, Appl. Phys. Lett. 36 (1980) 986.
[23] C. Leger, S. Bach, P. Soudan, J.-P. Pereira-Ramos, J. Electrochem. Soc. 152 (2005) A236.
[24] C. Leger, S. Bach, P. Soudan, J.-P. Pereira-Ramos, Solid State Ionics 176 (2005) 1365.